npj | climate and atmospheric science

www.nature.com/npjclimatsci

ARTICLE OPEN

Check for updates

Projected increase in summer heat-dome-like stationary waves over Northwestern North America

Ziming Chen[1]✉, Jian Lu[1]✉, Chuan-Chieh Chang[1], Sandro W. Lubis[1] and L. Ruby Leung[1]

Heat-dome-like stationary waves often lead to extreme heat events, such as the unprecedented heatwave in Northwestern North America during the summer of 2021. However, future changes in summer stationary waves over Northwestern North America and the underlying driving factors remain unclear. Here, we investigate the projected changes in the anticyclonic stationary wave circulation over Northwestern North America using data from the Coupled Model Intercomparison Project Phase 6 and diagnose the circulation changes using a stationary wave model. Our findings reveal a significant 95% increase in the summer stationary wave amplitude over Northwestern North America under the high-emission scenario in 2080–2099 relative to 1995–2014. The response is mainly driven by the diabatic heating changes over the tropical Pacific which induce a Rossby wave source in the northeastern tropical Pacific, and further supported by a northward expanded waveguide in North America, both enhancing wave activity flux into the Northwestern North America. The heat-dome-like stationary wave anomaly is expected to heighten the heatwave risk over the region.

npj Climate and Atmospheric Science (2023)6:194 ; https://doi.org/10.1038/s41612-023-00511-2

INTRODUCTION

Stationary waves are large-scale atmospheric circulation anomalies on monthly or longer time scales[1–4]. Stationary waves play an important role in shaping the regional climate and are responsible for many extreme weather events[2,5]. For example, an unprecedented heatwave in the Northwestern North American region in the summer of 2021[6,7] was associated with an anomalous anticyclonic (or heat-dome-like) circulation in the mid-upper troposphere[7–10], which resulted in ~1000 deaths and numerous wildfires[5,11,12]. The 1988 drought over the central United States and the catastrophic 2003 European heatwave were also associated with abnormal stationary waves in the upper troposphere[5,13–16]. Hence understanding and predicting the future changes in stationary waves are of critical importance.

Much attention has been given to the future projections of wintertime stationary waves because of their relatively large magnitude[1–3,17–22]. In general, an equivalent-barotropic response of stationary waves and an eastward phase shift are seen during the boreal winter with increasing carbon dioxide (CO_2) concentration[2,3,19,21]. Under high-emission scenarios, the wintertime stationary wave circulations at mid-high latitudes in the Northern Hemisphere are projected to be weakened to ~15–30% of the present-day climatology[2]. Compared to the changes in the wintertime stationary waves, the response of the summertime stationary waves has received less attention[2,5,23,24]. During boreal summer, the stationary wave circulation is projected to weaken in the tropics (30°S–30°N)[2]. This weakening is associated with an increase in moisture content and moist static energy (MSE) over the ocean due to tropical sea surface temperature (SST) warming, which reduces the land-sea MSE contrast and weakens the stationary wave circulation[24–28]. In addition, the projected decrease in zonal SST gradient over tropical Pacific contributes to the weakening of stationary wave intensity in the subtropical subsidence area by weakening the tropical overturning circulations[2,24]. On the other hand, warming of land surface temperature enhances the MSE thermal maximum and convective activity over land, which strengthens the stationary wave circulations. This effect partly offsets the impact of tropical SST warming by modulating the land-sea MSE contrast[29,30].

Unlike the tropics, the responses of the summertime stationary waves in the mid-latitudes (around 45°N) are different. In the upper troposphere over Northwestern North America, the probability of heat-dome-like anticyclonic circulation is projected to increase under the high-emission scenario[9]. But the projected increase in the probability is weak based on single-model ensemble dataset[9]. Nonlinear interactions between the upper-level stationary wave circulation and the soil moisture deficit would further increase the severity of heat extremes in the region[9,10,31]. About 40% of the extreme temperature anomaly in the 2021 Northwestern North America summer heatwave can be explained by the soil moisture-atmosphere interaction[10].

Despite the extensive research on the impact of stationary waves on heat extremes, the projected changes in stationary wave circulation over Northwestern North America and the underlying driving mechanisms remain unclear. Here, focusing on the projected changes in stationary wave circulation over Northwestern North America, we identify the dominant physical processes driving those changes. Our findings reveal a robust strengthening of the anticyclonic circulation in the upper troposphere by the end of the 21st century under the intermediate and high emission scenarios. Using a stationary wave model and utilizing Rossby wave ray tracing, the enhancements of the stationary wave can be attributed to the increase in diabatic heating over the tropical Pacific. By unraveling the dominant underlying dynamical mechanisms, we gain a better understanding of the cause of the projected changes in the stationary wave circulation and their implications for future heatwave changes.

[1]Atmospheric, Climate, & Earth Sciences (ACES) Division, Pacific Northwest National Laboratory, Richland, Washington, USA. ✉email: ziming.chen@pnnl.gov; jian.lu@pnnl.gov

RESULTS

A robust enhancement of anticyclonic stationary wave over Northwestern North America

To quantify the intensity of the anticyclonic stationary wave circulation over Northwestern North America, we define an eddy meridional wind dipole index as the difference in eddy meridional wind at 200 hPa between the western and eastern flanks of the anticyclonic circulation (boxed areas in Fig. 1a). Increasing trends in the dipole index are found in both the reanalysis dataset (1979–2018) and historical simulations of 26 CMIP6 models (1979–2014; Table S1), with statistical significance levels of 2% and 0.1% based on the nonparametric Mann-Kendall test (Fig. 1b).

The intensity of the anticyclonic stationary wave circulation over Northwestern North America is projected to continue to increase in the future. To illustrate the integrated characteristics of the large-scale circulations over North America in the future, we show the projected changes of the eddy meridional wind and eddy stream function for 2080–2099 under the high-emission Shared Socio-economic Pathways (SSP) 5–8.5 scenario (Figs. 1a and 2a–d). Compared to 1995–2014, robust positive and negative anomalies of eddy meridional wind at 200 hPa are found over northwestern and midwestern North America, respectively (Fig. 1a). More than 70% of the 26 climate models show agreement on the signs of meridional wind changes in both boxed areas (white dots in Fig. 1a). Correspondingly, a robust positive eddy stream function anomaly is found over Northwestern North America (Fig. 2c). This feature is relatively robust (as indicated by the white dots) and is accompanied by a positive eddy stream function anomaly over the northeast Pacific in the lower troposphere (Fig. 2d). To quantify the projected enhancement of the anticyclonic stationary wave, we calculate the relative percentage increase in the dipole index increase during 2080–2099 with respect to its mean state value in 1995–2014. The dipole index is projected to increase by 95% (with ±1-time inter-model standard deviation range from −36% to 226%) during 2080–2099 under the SSP5-8.5 scenario (Fig. 1b). Compared to previous projections based on CMIP5 models[2], our results based on CMIP6 models show a better agreement for the enhancement of the upper tropospheric stationary wave circulation over the Northwestern North America region.

Unlike Northwestern North America, a weakening subtropical high is projected over the North Pacific. Furthermore, similar to the response noted in previous studies focusing on the wintertime stationary waves[2,3], marked eastward shifts of cyclonic and anticyclonic circulations are seen over the northeastern Pacific in the upper and lower troposphere, respectively (Fig. 2c, d). The eastward shifts would strengthen the anticyclonic circulation over Northwestern North America, as the eastern flank of the cyclonic circulation system at 200 hPa over the northeastern Pacific increases the positive anomaly of eddy meridional wind over the western coast of Northwestern North America (Fig. 2a, c).

To demonstrate the dynamical control of stationary waves on the heat extremes, we regress the detrended anomalies of summer daily maximum temperature (Tmax) onto the detrended anomalies of the dipole index from 1979 to 2014 in the reanalysis dataset (Fig. 1c). The results show a significant positive anomaly of Tmax over Northwestern North America, suggesting that a stronger anticyclonic stationary wave circulation over Northwestern North America leads to a higher Tmax. Similar regression pattern of Tmax against the detrended dipole index is also obtained for the future climate (from 2050 to 2099) under both high-emission (Fig. 1d) and intermediate-emission (SSP2-4.5, Supplementary Fig. 1) scenarios. These results indicate a strong association between a more intense anticyclonic circulation and a higher Tmax over Northwestern North America in both the present-day climate and the projected warmed climate, via large-scale subsidence which would lead to cloud-free condition and persistent downward shortwave radiation[32]. This is further corroborated by the significant correlation between the dipole index and the Tmax averaged over Northwestern North America across models (Fig. 1e and Supplementary Fig. 1c). Hence the projected strengthening of the stationary wave circulation over Northwestern North America will strongly influence the local extreme heat events.

Given the significant impact of the enhanced stationary wave circulation on positive temperature anomalies in Northwestern North America, we are motivated to investigate the physical mechanism behind the stationary wave response in the CMIP6 models. To this end, a series of idealized experiments are conducted by using a stationary wave model[20], followed by a diagnostic analysis (Supplementary Table 3). A zonally varying control (CTRL) state is obtained by prescribing a zonally asymmetric basic state and forcing it with three-dimensional diabatic heating and transient eddy forcings derived from the historical simulations of the CMIP6 models during 1995 to 2014. To simulate the projected stationary wave circulation of the CMIP6 climate models under the SSP5-8.5 scenario during 2080–2099, we prescribe the same basic states as in the CTRL run, while forcing it with the projected asymmetric forcings (the resulting solution is referred to as PROJ).

The CTRL run reproduces the mean states of the upper- and lower-level stationary wave circulation simulated by the CMIP6 models reasonably, while a southeastward bias of eddy meridional wind at 200 hPa over North America is found compared to the reanalysis dataset (Supplementary Fig. 3). Contrasting against CTRL, the PROJ run is intended to capture the stationary wave response of the comprehensive climate models using the idealized dry stationary wave model and attribute the response to different forcing mechanisms. Comparing the right and left columns in Fig. 2, the PROJ run of the stationary wave model can roughly capture the projected anticyclonic stationary wave circulation anomaly over the Northwestern North America in the CMIP6 multi-model mean (MMM), although considerable difference is apparent between the stationary wave model and CMIP6 MMM. The pattern correlation coefficient (PCC) and root-mean-square error (RMSE) of the eddy stream function at 200 hPa between the CMIP6 MMM projection and the PROJ run of the stationary wave model are 0.84 and 2.81×10^6 m^2 s^{-1}, respectively (Fig. 2g). The stationary wave model exhibits even higher skill in simulating the response at 850 hPa, with a PCC of 0.95 and a RMSE of 0.59×10^6 m^2 s^{-1} (Fig. 2h). The better performance of the stationary wave model in the lower troposphere can be attributed to the projected diabatic cooling over the northeastern Pacific (Supplementary Fig. 8c), which triggers an anomalous anticyclonic circulation over western North America[33], in line with the Gill's model solution[34]. Unlike the eddy stream function anomalies, the anticyclonic anomalies at 200 hPa over the North American continent exhibit a southeastward shift and an exaggeration in the PROJ run relative to the CMIP6 MMM. These limitations may stem from the southward and southeastward biases in the westerly jet and eddy meridional wind over the western contiguous U.S. in the CTRL run of the stationary wave model, respectively (Supplementary Figs. 3 and 9). These discrepancies may also arise from the complex interplay between the transient eddies, stationary waves, and diabatic heating within the CMIP6 models, which cannot be fully captured by the stationary wave model.

The dominant role of diabatic heating over tropical Pacific

To better delineate the relative importance of the different drivers of the stationary wave response, the relative contributions of the diabatic heating and transient forcings are examined through a series of sensitivity runs: diabatic heating run, transient vorticity (TF_v) run and transient divergence (TF_D) run (Supplementary Table 3). In each experiment, the forcing of interest is fixed at its

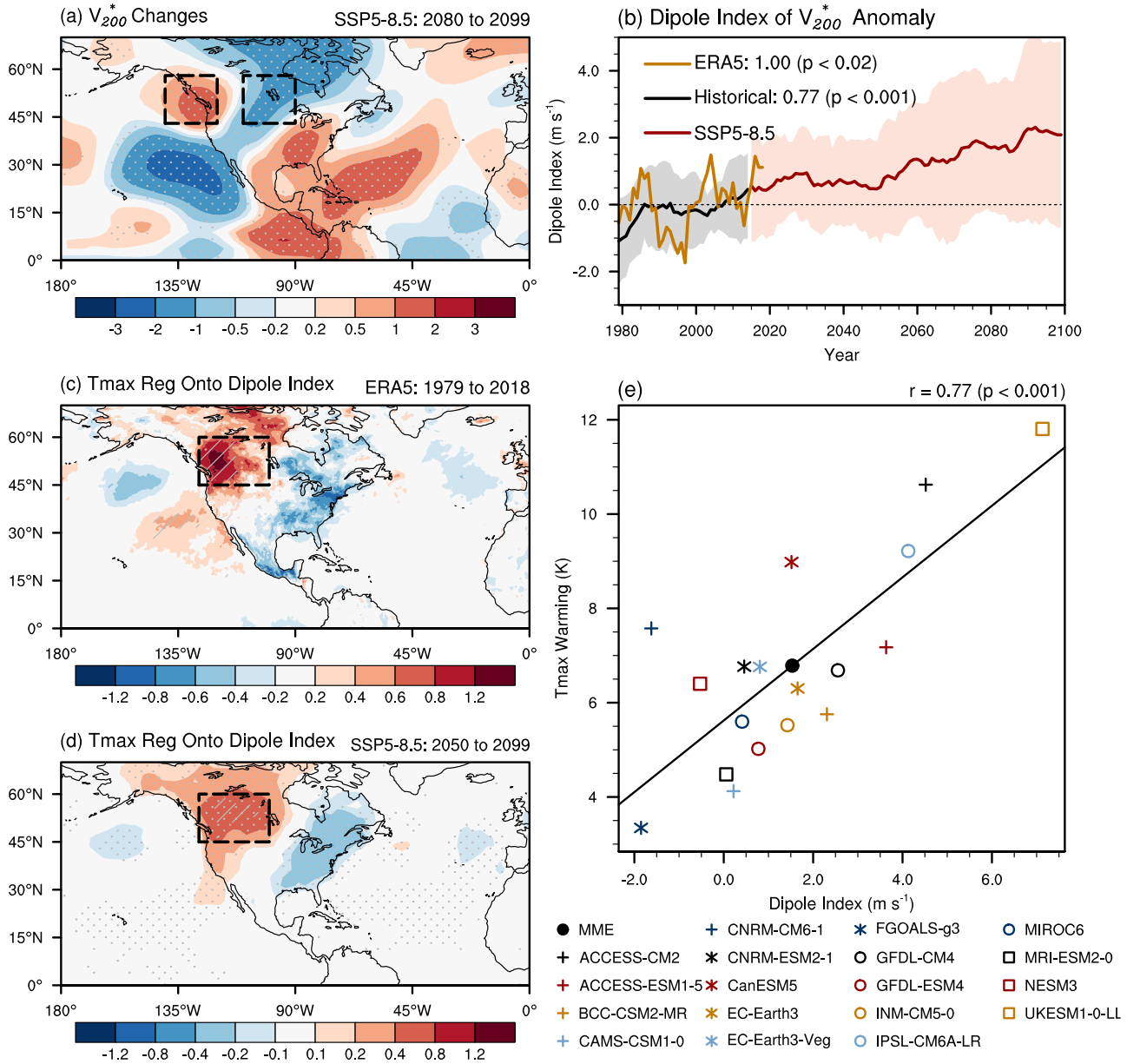

Fig. 1 Changes in the upper-tropospheric circulation pattern and its impact on the summer daily maximum temperature (Tmax) over the Northwestern North America. a The projected changes of the eddy meridional wind at 200 hPa during the boreal summer (June to August) in 2080–2099 relative to 1995–2014 under SSP5–8.5 (units: m s^{-1}). **b** The dipole index of the eddy meridional wind anomaly (units: m s^{-1}). The dipole index is defined as the difference between the western (43°N–58°N, 120°W–140°W) and eastern (43°N–58°N, 90°W–110°W) areas indicated by the black dashed boxes in (**a**). The yellow line shows the time series of the dipole index anomaly in the fifth-generation atmospheric reanalysis of the European Centre for Medium-Range Weather Forecasts (ERA5), while the black and red lines show the historical and projected time series, respectively, simulated by 26 CMIP6 models under the SSP5-8.5 (see Data and Methods). Shading represents the range of ±1 standard deviation across models. The linear trend of the dipole index and the nonparametric Mann-Kendall significance level for ERA5 and historical simulations are also marked. **c** Regression of the detrended daily maximum temperature (Tmax) anomaly onto the detrended and standardized dipole index in the ERA5 from 1979 to 2018. **d** The projected changes in detrended Tmax regressed onto the standardized projected changes in the detrended dipole index from 2050 to 2099 under SSP5-8.5 scenario. After detrending Tmax and the dipole index, we calculate the regression for each CMIP6 model and compute the multimodel mean. **e** The intermodel scatter between the changes in the dipole index and Tmax averaged over Northwestern North America (black dashed box in (**b**, **c**)) between 2080–2099 and 1995–2014. A regression line obtained by the least squares method is also shown, with the correlation coefficient and significant level marked at the top of the panel. The white dot in (**a**–**d**) indicates regions where at least 70% of the models agree on the sign of the projected change or the regression coefficient. Hatching in (**c**) indicates the regression coefficients are significant at the 90% confidence level of Student's *t*-test, while hatching in (**d**) indicates the regression coefficients in more than half of the models exceed the 90% confidence level of the Student's *t*-test.

historical values, while all other forcings are the same as the PROJ run to account for the possible interaction among different forcings[35]. The contribution of the forcing of interest can thus be isolated as the difference between the PROJ and sensitivity runs. The results show that diabatic heating dominates the projected changes of eddy meridional wind and eddy stream function at 200 hPa, with PCC values of 0.98 and 0.99 between the response due to diabatic heating and that in PROJ run, respectively, while

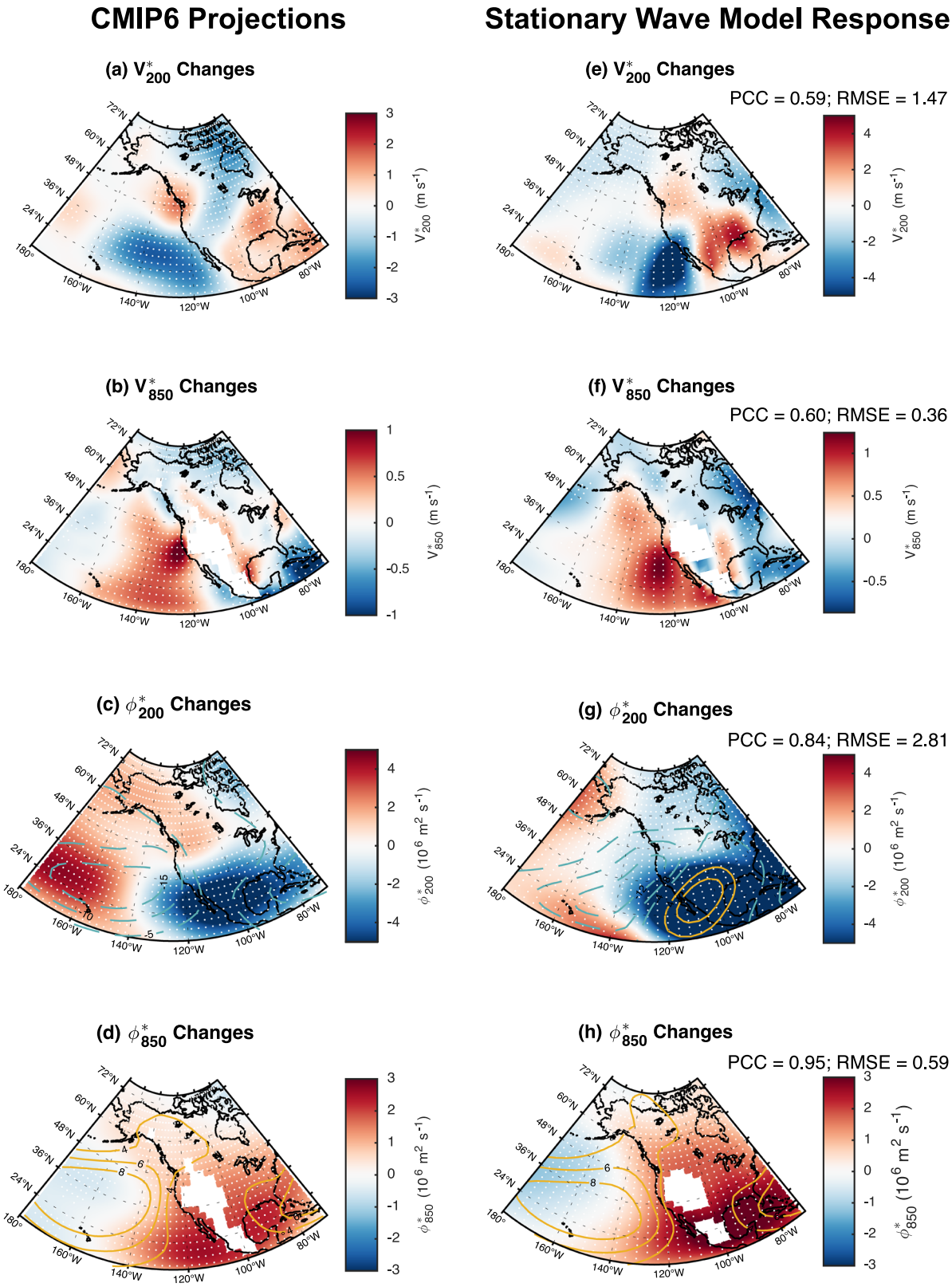

vorticity forcing only partly offsets the diabatic heating effect (Fig. 3 and Supplementary Fig. 4). Similar cancellation effect of vorticity forcing can be found at 850 hPa (Supplementary Fig. 5).

Given the significant impact of diabatic heating, it is important to isolate its dominant sources. Further experiments driven by the diabatic heating from different broad regions, including the tropics (20°S–20°N), northern subtropics (20°N–40°N), and mid-high latitudes (40°S–70°N) are conducted. The results show that both tropical and subtropical diabatic heating contribute equally to the projected stationary wave responses over Northwestern

Fig. 2 Projected changes in the boreal summer stationary wave by the CMIP6 models and the stationary wave model. a, **b** the CMIP6 projected changes in the eddy meridional wind at 200 hPa and 850 hPa in 2080–2099 relative to 1995–2014 under SSP5-8.5, respectively (units: m s^{-1}). Similarly, (**c**, **d**) depict the CMIP6 projected changes in the eddy stream function (units: 10^6 m^2 s^{-1}). The solid and dashed contours in (**c**, **d**) represent the climatology for the period of 1995–2014. The white dots denote consistent sign of projected changes across >70% of the models. **e**–**h** correspond to (**a**–**d**), respectively, but for the responses obtained from the projection run of stationary wave model (PROJ; Supplementary Table 3). The solid and dashed contours in (**g**, **h**) represent the climatology of the eddy stream function in the control run of stationary wave model (CTRL). The white dots denote a response that exceeds the noise of stationary wave model (see Methods). The pattern correlation coefficient (PCC) and root-mean-square error (RMSE) between the CMIP6 projected changes and the stationary wave model responses are indicated in the top-right corner of (**e**–**h**).

North America (Supplementary Figs. 6 and 7). Further disaggregating the tropical and subtropical forcings into smaller subregions for the stationary wave model experiments, we find that the diabatic heating in the tropical Pacific emerges as the most predominant driver for the aforementioned stationary wave feature in the upper troposphere (PCC = 0.87; Fig. 4a), while the diabatic heating localized to the North American continent (PCC = 0.33) and the diabatic heating from the north Atlantic (PCC = 0.53) only contribute secondarily (Fig. 4).

The contribution of wave source over the tropical Pacific

Diagnosis using the stationary waves model reveals the dominant role of the tropical Pacific heating in driving the enhancement of the stationary waves over Northwestern North America at the end of the 21st century. However, the tropical Pacific exhibits broad regions of both positive and negative diabatic heating changes (Fig. 4g and Supplementary Fig. 8), which may have different impacts on stationary waves over the Northwestern North America region. This motivates us to further explore the underlying teleconnection mechanism that links the tropical heating to the projected changes in the stationary wave over Northwestern North America.

Considering that Rossby waves propagate along the waveguide of the westerly jet[36,37], we compare the waveguide effect on Rossby wave propagation between the future climate and the present-day climate simulated by the CMIP6 models, as measured by a stationary zonal wavenumber defined on the Mercator projection (Fig. 5a; See Methods). In the present-day climate, a high stationary zonal wavenumber tongue is seen over the tropical northeastern Pacific (black dashed box in Fig. 5a). Here waveguide is defined as the region with positive stationary wavenumber, following Hoskins[37]. In a changing climate, the stationary wave number over the United States is projected to increase, suggesting that the extent of the waveguide will expand (blue box in Fig. 5a). Since the waveguide is closely related to the location of the westerly jet[37], the expansion of the waveguide over North America is linked to the poleward shift of the westerly jet (Supplementary Fig. 9a), which has been found to be a robust feature of the projected westerly wind change over the eastern Pacific-North America sector during the boreal summer[38]. The expansion of the waveguide there favors a more northward propagation of Rossby waves into Northwestern North America under the changing climate (Fig. 5b).

In addition to the waveguide expansion above, the wave source is projected to increase robustly over the tropical northeastern Pacific (negative values in the black dashed box of Fig. 5c, see Methods), primarily due to the increase in diabatic heating over the tropical Pacific. The mid-to-upper troposphere exhibits a pronounced enhancement of diabatic heating over the tropical and northern Pacific, which dominates the projected changes in the vertically integrated diabatic heating changes (Supplementary Fig. 8). The pronounced increase of diabatic heating over the eastern equatorial Pacific (0°–10°N, 150°W–90°W; yellow box in Supplementary Fig. 8) and decrease over the tropical northeastern Pacific (10°N–25°N, 120°W–90°W; gray box in Supplementary Fig. 8) result in anomalous easterly and westerly winds at 200 hPa over the tropical northeastern Pacific, giving rise to a positive divergence anomaly (Supplementary Fig. 9a).

Since the Rossby wave source is associated with divergent flow and absolute vorticity (See Methods), the positive divergent flow anomalies will then lead to an enhancement of the wave source. To identify the impact of divergent flow on the wave source and the teleconnection that links the tropical Pacific heating to the stationary wave changes over Northwestern North America, we show the projected changes of wave source and the relative contribution of divergent flow and absolute vorticity (Supplementary Fig. 10; See Methods). By sign convention, a negative anomaly of $\nabla \cdot (\overline{v}_\chi \xi)$ corresponds to a positive Rossby wave source anomaly in the Northern Hemisphere, and vice versa[39]. For the projection period under the SSP5-8.5 scenario, the divergent flow shown in Supplementary Fig. 10 contributes to the enhancement of the wave source over the tropical northeastern Pacific (Fig. 5c).

As a result of both the waveguide expansion (Fig. 5a) and the enhanced wave source (Fig. 5c), more northward wave activity flux is found over the Pacific coast of the United States under the changing climate (vectors in Fig. 5c). This enhanced wave activity flux feeds into Northwestern North America, helping the buildup of the anticyclonic circulation there. These diagnostic results from the CMIP6 model simulations are consistent with the wave behavior in the stationary wave model forced by the tropical Pacific heating (cf. Supplementary Figs. 9 and 11), demonstrating the robustness of the physical mechanism.

DISCUSSION

Heatwaves are often associated with heat-dome-like stationary wave circulations in the upper troposphere[5,9,10]. For example, an unprecedented heatwave hit Northwestern North America from late June to early July in 2021, causing severe regional impacts on the society and ecosystem[6–8]. Understanding the projected changes of heat-dome-like stationary wave circulation is crucial for adapting to and mitigating the impacts of future heatwaves. In this study, we find that the heat-dome-like stationary wave circulation in the upper troposphere over Northwestern North America is projected to double (~95%) in magnitude by the end of the 21st century under the high-emission scenario. Sensitivity experiments using the stationary wave model isolate the diabatic heating from the tropical eastern Pacific as the dominant driver. The dipole changes in diabatic heating over the tropical eastern Pacific lead to an enhancement of the wave source over the tropical northeastern Pacific, triggering amplified Rossby waves that propagate towards Northwestern North America, with assistance from a poleward expanded waveguide. Similar dynamical processes can be captured by the idealized model forced by the tropical diabatic heating, providing a dynamical rationale for the confidence in the future increase of heat-dome-like stationary wave circulation over Northwestern North America.

We find a noticeable projection uncertainty in the projected changes of the stationary wave circulation. To investigate the potential sources of this uncertainty, we compare the changes in the eddy meridional wind at 200 hPa and vertically averaged diabatic heating, and the relative SST warming projected by the

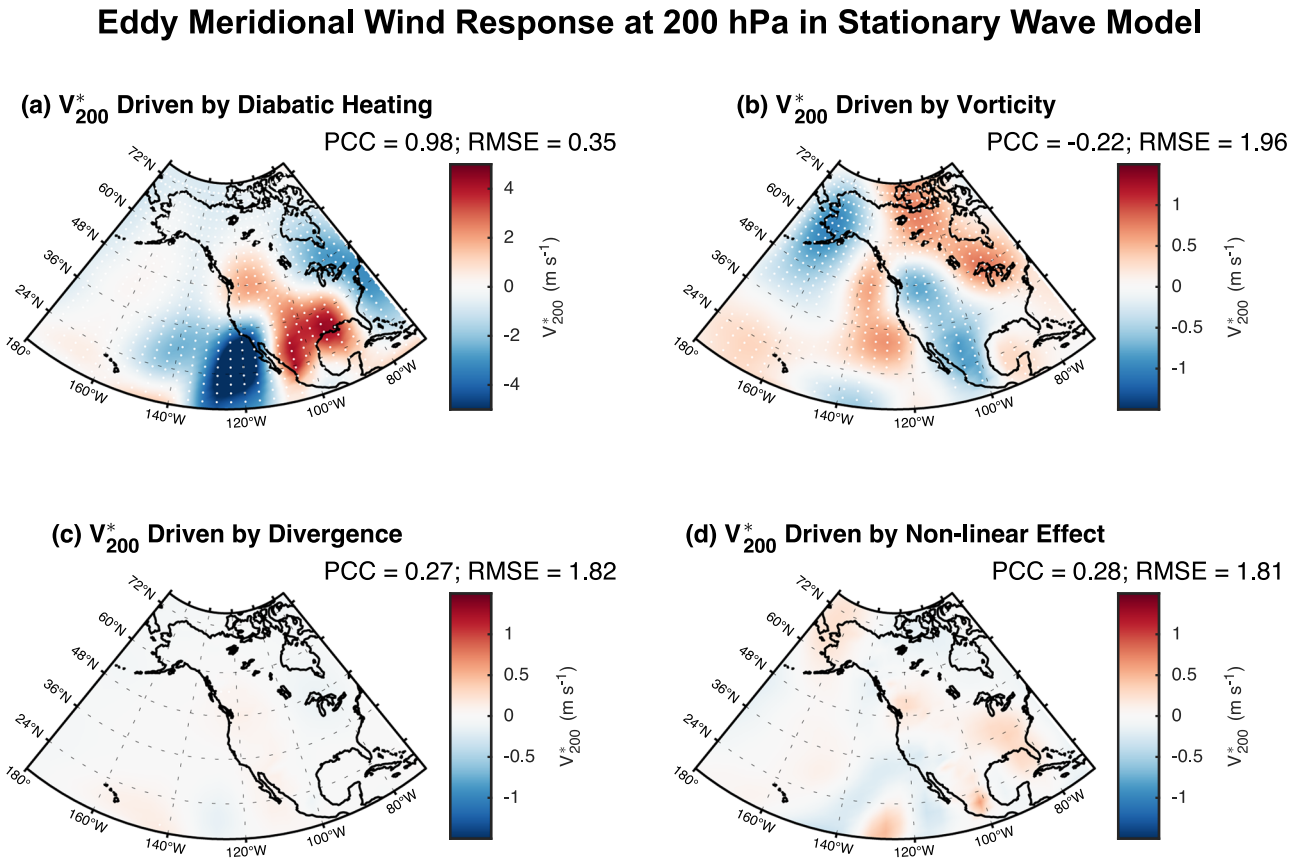

Fig. 3 The stationary wave model response of eddy meridional wind at 200 hPa to different forcings. The response is contributed by (**a**) diabatic heating, (**b**) vorticity, (**c**) divergence, and (**d**) non-linear effect. The pattern correlation coefficients (PCCs) and root-mean-square errors (RMSEs) between the response of the PROJ run of the stationary wave model and that to specific forcing as isolated via sensitivity runs are indicated in the top-right corner. The white dots denote a response that exceeds the noise of stationary wave model (see Methods).

models with increasing and decreasing dipole index, respectively (Supplementary Fig. 12). A positive anomaly of diabatic heating over the tropical Pacific is found in the model group with increasing dipole index, while the increase of heating is much weaker in the model group with decreasing dipole index. Hence the projection uncertainty in the stationary wave circulation over Northwestern North America may be closely related to uncertainty in the projected changes in tropical diabatic heating.

The projected change in tropical diabatic heating is likely related to tropical air-sea interactions under the influence of increasing greenhouse gas forcing, particularly the El Niño-like warming in the eastern equatorial Pacific[40,41]. Our results show that the El Niño-like warming pattern would enhance the tropical diabatic heating in the projection (Supplementary Fig. 12b). During the boreal summer, the enhanced equatorial warming extends equatorward, resulting in expansion of the eastern Pacific Intertropical Convergence Zone[38,40,41] and the equatorial heating anomalies shown in Fig. 4g. Therefore, the ultimate source of the anticyclonic stationary wave response of Northwestern North America can be traced back to the change in the coupling of the ocean-atmosphere system, which remains an important source of uncertainty[40,42–44]. In addition, local nonlinear interactions between soil moisture and atmospheric circulation can enhance the anticyclonic stationary wave circulation and heatwaves as found for the case of the Northwestern North America heatwave in the summer of 2021[10,31]. Further studies are needed to determine the relative contributions of tropical diabatic heating resulting from atmosphere-ocean coupling and local land-atmosphere feedback to the projected changes in heat-dome-like stationary wave circulation and heatwaves over Northwestern North America.

At the intraseasonal scale, we further analyze the daily outputs from CMIP6 models and find a significant increase in the frequency of occurrence of the positive dipole index during the boreal summer in 2080–2099 under the SSP5-8.5 scenario, compared to 1995–2014 (Supplementary Fig. 13). Interestingly, the robust increase is not found in other seasons. These suggest that we would experience more intense and frequent heat-dome-like weather patterns during the boreal summer over Northwestern North America in the future.

In summary, our study demonstrates a robust enhancement of anticyclonic stationary wave circulation over Northwestern North America across the CMIP6 models. Although the underlying cause of the robust changes in the stationary wave circulation remains to be understood, it is likely tilting the circulation distribution over Northwestern North America to be more favorable for heatwaves, thereby amplifying the mean warming effect of the increasing greenhouse gases. Further studies are needed to explore the stationary wave response and the associated effects over other regions.

METHODS

Data

This study used the monthly and daily datasets of the fifth-generation atmospheric reanalysis of the European Centre for Medium-Range Weather Forecasts (ERA5), with a spatial resolution of $0.25° \times 0.25°$ and 137 levels from the surface up to a height of 80 km for the period of 1950 to present[45].

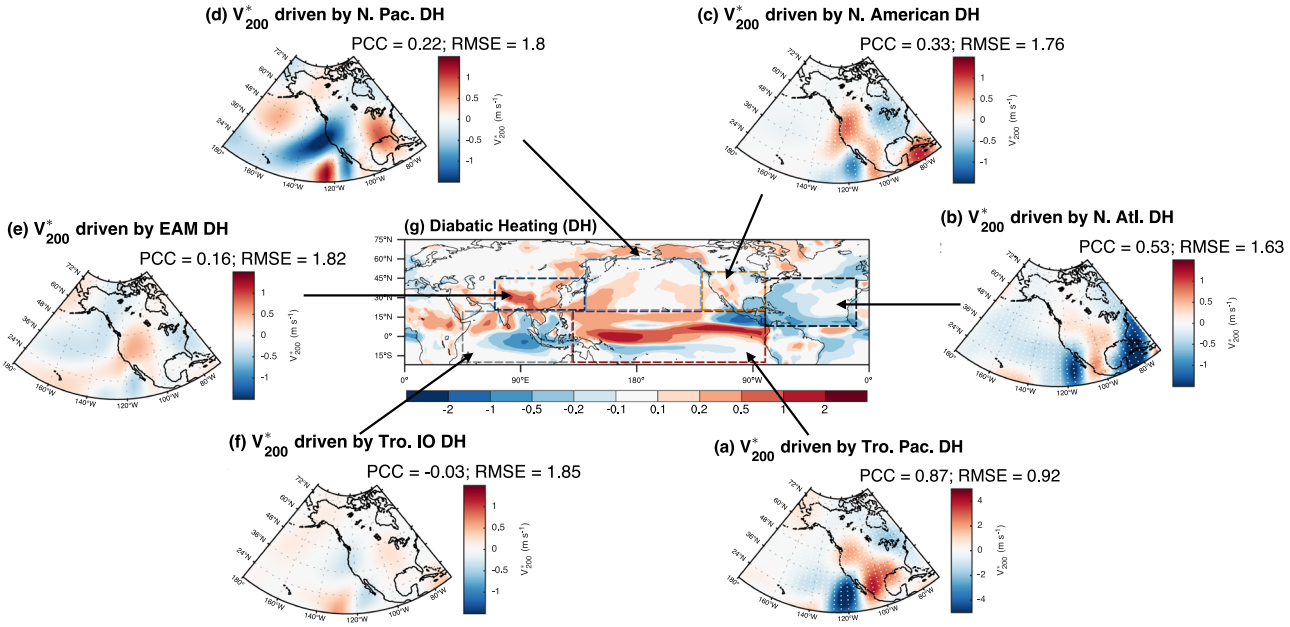

Fig. 4 The contribution of diabatic heating (DH) in different regions to the stationary wave changes projected by the stationary wave model. The 200 hPa eddy meridional wind responses simulated by the stationary wave model driven by the diabatic heating in the (**a**) tropical Pacific (Tro. Pac.; 20°S–20°N, 130°E–80°W), (**b**) North Atlantic (N. Atl.; 8°N–45°N, 10°W–80°W), (**c**) North America (N. America; 20°N–50°N, 130°W–80°W), (**d**) North Pacific (N. Pac.; 20°N–60°N, 140°E–130°W), (**e**) East Asian monsoon region (EAM; 20°N–45°N, 70°E–140°E), (**f**) tropical Indian Ocean (Tro. IO; 20°S–20°N, 45°E–130°E) (units: m s^{-1}). The white dots denote a response that exceeds the noise of stationary wave model (see Methods). **g** Vertically averaged diabatic heating changes under the SSP5-8.5 scenario for the period of 2080–2099 (units: K day^{-1}). The pattern correlation coefficients (PCCs) and root-mean-square errors (RMSEs) between the response in the PROJ and the sensitivity runs of stationary wave model are shown in the top-right corner.

To identify the projected stationary wave changes, we use the monthly output from 26 CMIP6 models (Supplementary Table 1), and the daily output from 18 CMIP6 models (Supplementary Table 2) including their historical simulations, and future projections under SSP2-4.5 and SSP5-8.5 scenarios[46,47]. We mainly describe the results of the high-emission scenario (SSP5-8.5), while the results of the intermediate-emission scenario are presented in the Supplementary Information. The first available realization for each model is used to give equal weight to each model. All the data are re-gridded to 2.5° × 2.5° grids using first-order conservative interpolation, except for the circulation patterns which are re-gridded using bilinear interpolation.

Description and experiment design of stationary wave model

The stationary wave model[20] is used to investigate the physical mechanisms responsible for the projected changes of stationary wave and related large-scale circulation. The stationary wave model is a time-dependent baroclinic model, which solves the three-dimensional (3D) nonlinear primitive equations for deviations from the basic states in response to zonally asymmetric imposed forcings on sigma coordinates. The basic states include horizontal winds, air temperature and surface pressure. The forcings include diabatic heating, transient fluxes (transient vorticity and transient divergence), and orography. The stationary wave model has rhomboidal wavenumber-30 truncation in the horizontal (~2.25° latitude × 3.75° longitude) and 24 unevenly spaced sigma levels in the vertical direction (R30L24). In addition, various damping terms are used in the stationary wave model to suppress model-generated transients and obtain a quasi-steady solution. The damping terms include Newtonian cooling, Rayleigh friction, and biharmonic diffusion, which are the same as those used by previous studies[3,48].

We prescribe the 3D basic states which are derived from the outputs of 26 CMIP6 models in the historical (1995–2014) and future (2080–2099) period, respectively. The 3D diabatic heating (DH, units: K day^{-1}) is diagnosed as a residual in the thermodynamic equation by using the analyzed vertical velocity from 14 CMIP6 models[49–51]:

$$DH = \frac{\partial T}{\partial t} + \overline{\mathbf{v}} \cdot \nabla \overline{T} + \left(\frac{p}{p_0}\right)^{\frac{R}{C_p}} \overline{\omega} \frac{\partial \overline{\theta}}{\partial p} + \left(\frac{p}{p_0}\right)^{\frac{R}{C_p}} \left[\nabla \cdot \overline{\mathbf{v}'\theta'} + \frac{\partial(\overline{\omega'\theta'})}{\partial p}\right], \quad (1)$$

where v denotes the horizontal wind vector, θ and T denote the potential temperature and air temperature, respectively ($\theta = T\left(\frac{p_0}{p}\right)^{R/C_p}$), ω denotes the pressure vertical velocity. R is the gas constant of air, and C_p is the specific heat capacity at a constant pressure. The overbar denotes the monthly mean, and the prime denotes the deviation of the daily mean from the monthly mean, viz. the transient component. Hence the transient component represents both synoptic and submonthly fluctuations. The transient vorticity (TF_v) and divergence (TF_D) fluxes are calculated by using the 3D daily mean wind fields from the 14 CMIP6 models:

$$TF_v = -\frac{\partial \overline{\zeta' u'}}{\partial x} - \frac{\partial \overline{\zeta' v'}}{\partial y} - \left[\frac{\partial}{\partial x}\left(\overline{\omega' \frac{\partial v'}{\partial p}}\right) - \frac{\partial}{\partial y}\left(\overline{\omega' \frac{\partial u'}{\partial p}}\right)\right], \quad (2)$$

$$TF_D = \frac{\partial \overline{\zeta' v'}}{\partial x} - \frac{\partial \overline{\zeta' u'}}{\partial y} - \frac{\partial}{\partial x}\left(\overline{\omega' \frac{\partial u'}{\partial p}}\right) - \frac{\partial}{\partial y}\left(\overline{\omega' \frac{\partial v'}{\partial p}}\right) - \frac{\partial^2}{\partial x^2}\left[\frac{1}{2}\left(\overline{u'^2} + \overline{v'^2}\right)\right] - \frac{\partial^2}{\partial y^2}\left[\frac{1}{2}\left(\overline{u'^2} + \overline{v'^2}\right)\right], \quad (3)$$

where u and v are the 3D zonal and meridional wind, respectively. $\zeta = \frac{\partial v}{\partial x} - \frac{\partial u}{\partial y}$, denoting the relative vorticity.

We calculate the diabatic heating and transient momentum fluxes for individual CMIP6 models before taking the multi-model mean (MMM). The MMM of basic states and forcings are first calculated on the pressure levels and then linearly interpolated onto the model sigma levels. The stationary wave model is integrated for 100 days, and the averaged value from the 30th to

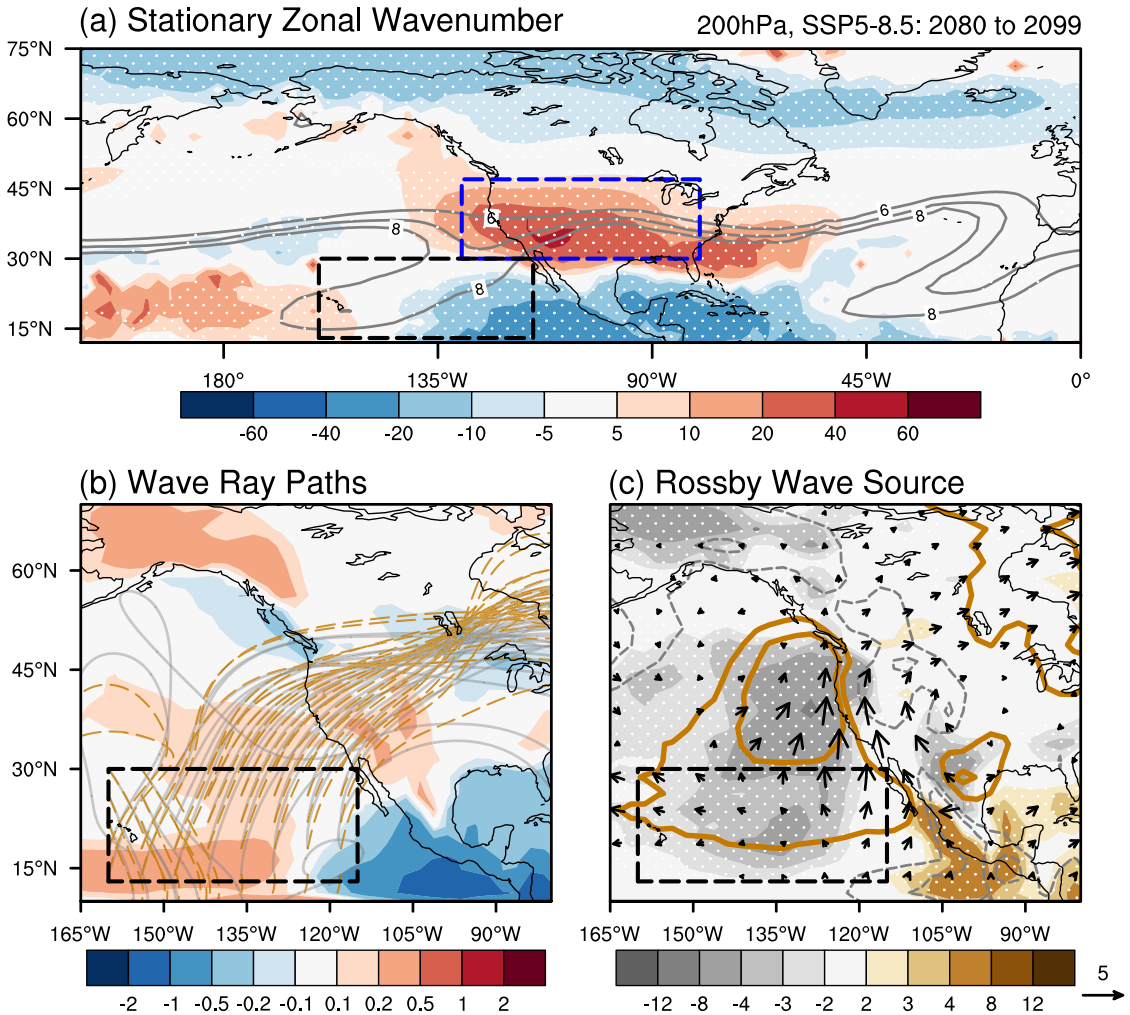

Fig. 5 The CMIP6 projected changes of Rossby waveguide, wave source, and stationary wave activity in the upper troposphere in 2080–2099 under the SSP5-8.5 scenario. a The projected percentage change of stationary zonal wavenumber (K_s) at 200 hPa in boreal summer (shading; units: %) and the spatial pattern of K_s in the historical simulation of 1995–2014 (contour; units: 1). The K_s represents the Rossby waveguide. The contour lines are 6, 7, 8. The gray solid and yellow dashed streamlines in (**b**) represent the pathway of Rossby wave propagation in the first 10 days after formation emanating from the black-box region (13°N–30°N, 160°W–115°W) under historical and SSP5-8.5 scenarios, respectively. Given the initial location (black box in (**b**)), its displacement is integrated for 10 days. The shading in (**b**) shows the projected changes in vertical averaged diabatic heating throughout the entire troposphere (units: K day^{-1}). The shading and vectors in (**c**) show the projected changes in the Rossby wave source (units: 10^{-11} s^{-2}) and wave activity flux (vector, units: m^2 s^{-2}) at 200 hPa, respectively. The gray and yellow contours represent the present-day climatology of Rossby wave source and wave sink, respectively. The contour values of the present-day wave source (wave sink) are −10 and −5 (5 and 10) × 10^{-11} s^{-2}. The blue box in (**a**) denotes the region where the waveguide is projected to expand, while the black box in (**a**–**c**) denotes the wave source where the Rossby wave will propagate to Northwestern North America. The white stippling denotes the same sign of projected changes in >70% of the models.

100th day is shown, given that a quasi-steady state would be reached by the 30th day[3,20].

To simulate the present-day climatology and the projected changes of stationary wave, the stationary wave model is driven by the forcings in historical (CTRL) and projection (PROJ) periods, respectively (Supplementary Table 3). In the CTRL run, by prescribing the three-dimensional basic states, the three-dimensional circulation patterns are obtained as forced by the present-day diabatic heating, TF_v, and TF_D fluxes. The projected circulation patterns in the PROJ run are obtained as forced by the projected diabatic heating, TF_v, and TF_D fluxes. To investigate the dominant forcing responsible for the projected changes of stationary wave, we design three sensitivity experiments to probe the importance of diabatic heating, TF_v, and TF_D, respectively, in the full stationary wave model response. To take into account the interaction between diabatic heating, TF_v and TF_D, the forcing of interest is fixed at its historical values, while the other two forcings in the PROJ run are used[35] (Supplementary Table 3). The single-forcing response is defined as the difference between the PROJ and sensitivity runs. In addition, the nonlinear effect is defined as the response difference between the PROJ run and the sum of the three sensitivity runs. To examine the significance of response in the PROJ run, we define the noise of stationary wave model as twice the standard deviation computed from the 30th to the 100th day.

Diagnostic method for the Rossby wave propagation and ray tracing

The characteristics of Rossby wave propagation are mainly determined by the zonal wind in the upper troposphere[37]. To identify the contribution of zonal wind driven by diabatic heating on the Rossby wave propagation, we calculate the stationary wavenumber K_s on the Mercator projection, which shows the

qualitative behavior of Rossby wave, following Karoly[52] and Hoskins and Ambrizzi[37]:

$$K_s = \left(\frac{a\beta_M}{\overline{v}}\right)^{1/2}, \tag{4}$$

$$\beta_M = \left[2\Omega - \left(\frac{1}{\cos\varphi}\frac{\partial}{\partial\varphi}\right)^2(\overline{v}\cos^2\varphi)\right]\left(\frac{\cos^2\varphi}{a}\right), \tag{5}$$

where $\overline{v} = \overline{U}/(a\cos\varphi)$ represents the relative rotation rate of the atmosphere, φ represents the latitude, a represents the Earth's radius, $\overline{U}$ represents the zonal wind at 200 hPa in the boreal summer, and Ω represents the Earth's rotational constant. The overbar denotes a time mean. β_M is the meridional gradient of absolute vorticity in the spherical coordinates.

The variation of stationary waves over northwestern North America may be preceded by an upstream Rossby wave train that extends from the tropical Pacific. To identify the wave source location in present day and projection period, we calculate the Rossby-wave source, following Sardeshmukh and Hoskins[39]:

$$S = -\nabla\cdot(\boldsymbol{v}_\chi\xi), \tag{6}$$

where $\boldsymbol{v}_\chi$ is the divergent flow and ξ is the absolute vorticity. The projected changes in Rossby-wave source (S') is contributed from the changes in divergent flow ($\boldsymbol{v}'_\chi$) and absolute vorticity (ξ'):

$$S' = -\nabla\cdot(\boldsymbol{v}'_\chi\overline{\xi}) - \nabla\cdot(\overline{\boldsymbol{v}_\chi}\xi') - \nabla\cdot(\boldsymbol{v}'_\chi\xi') + \mathrm{Res}, \tag{7}$$

where Res denotes the residual term, and $-\nabla\cdot(\boldsymbol{v}'_\chi\overline{\xi})$ and $-\nabla\cdot(\overline{\boldsymbol{v}_\chi}\xi')$ represent the contribution from the changes in divergent flow and absolute vorticity, respectively.

To measure the wave propagation, we calculate the wave activity flux, following Plumb[53]. The wave activity flux represents the 3D propagation of the stationary Rossby waves[53]. The horizontal components in pressure coordinates are:

$$F_s = p\cos\varphi\begin{pmatrix}\frac{1}{2a^2\cos^2\varphi}\left[\left(\frac{\partial\phi'}{\partial\lambda}\right)^2 - \phi'\frac{\partial^2\phi'}{\partial\lambda^2}\right]\\ \frac{1}{2a^2\cos^2\varphi}\left[\frac{\partial\phi'}{\partial\lambda}\frac{\partial\phi'}{\partial\varphi} - \phi'\frac{\partial^2\phi'}{\partial\lambda\partial\varphi}\right]\end{pmatrix}, \tag{8}$$

where ϕ' represents the eddy stream function, and λ represents the longitude.

In addition, to figure out the ray pathway of Rossby wave propagation, we use a wave ray tracing technique developed by Li[54] and Zhao[55]. By accounting for the meridional wind in the mean state, a two-dimensional wave dispersion relationship for a horizontally nonuniform flow in the ray-tracing algorithm is used on a beta plane:

$$\Omega = \overline{U}k + \overline{V}l + \frac{\overline{q}_x l - \overline{q}_y k}{k^2 + l^2}, \tag{9}$$

where Ω, k, and l are the angular frequency, zonal and meridional wavenumbers, respectively. $\overline{V}$ is the basic state of meridional wind at 200 hPa in the boreal summer. A spectral triangular truncation at wavenumber 11 is used to smooth the background flow. The $\overline{q}_x$ and $\overline{q}_y$ represent the zonal and meridional gradients of absolute vorticity, respectively. Given that we focus on the stationary wave in the upper troposphere, Ω is set 0. The initial zonal wave number is set as 4. When we get the initial k and m, the initial meridional wavenumber can be calculated by solving Eq. (9). The zonal and meridional components of group velocity can be expressed as:

$$\frac{d_g x}{dt} = c_{g,x} = \overline{U} + \left(\left(k^2 - l^2\right)\overline{q}_y - 2kl\overline{q}_x\right)/K^4, \tag{10}$$

$$\frac{d_g y}{dt} = c_{g,y} = \overline{V} + \left(\left(k^2 - l^2\right)\overline{q}_x + 2kl\overline{q}_y\right)/K^4, \tag{11}$$

where K^2 represents the total wavenumber $\left(K^2 = \frac{\overline{q}_y k - \overline{q}_x l}{\overline{U}k + \overline{V}l}\right)$, while $\frac{d_g}{dt} = \frac{\partial}{\partial t} + c_{g,x}\frac{\partial}{\partial x} + c_{g,y}\frac{\partial}{\partial y}$ represents the Lagrangian variation moving at the group velocity. x and y are the longitude and latitude of rays at time step t. By using the initial location of the ray pathway, the displacement of ray pathway can be calculated by the fourth order Runge-Kutta method[56] and integrated for 10 days.

CODE AVAILABILITY

The data in this study is analyzed with NCAR Command Language (NCL) and Matlab R2021b. The relevant codes in this work are available, upon request, from the corresponding author Z.C. and J.L.

DATA AVAILABILITY

Stationary wave model outputs are available on request from Z.C. and J.L. All other datasets used in this study are freely available for download from Earth System Grid Federation (ESGF; https://esgf-node.llnl.gov/projects/cmip6/) or European Centre for Medium-Range Weather Forecasts (https://www.ecmwf.int/en/forecasts).

Received: 12 July 2023; Accepted: 24 October 2023;
Published online: 21 November 2023

REFERENCES

1. Held, I. M., Ting, M. & Wang, H. Northern winter stationary waves: theory and modeling. *J. Clim.* **15**, 2125–2144 (2002).
2. Wills, R. C. J., White, R. H. & Levine, X. J. Northern Hemisphere stationary waves in a changing climate. *Curr. Clim. Chang. Rep.* **5**, 372–389 (2019).
3. Simpson, I. R., Seager, R., Ting, M. & Shaw, T. A. Causes of change in Northern Hemisphere winter meridional winds and regional hydroclimate. *Nat. Clim. Chang.* **6**, 65–70 (2016).
4. Nigam, S. & DeWeaver, E. Stationary waves (orographic and thermally forced). in *Encyclopedia of Atmospheric Sciences* 2nd edn, Vol. 5th (ed. Holton, J. R.) Ch. 2121–2137 (Elsevier, 2003).
5. White, R. H., Kornhuber, K., Martius, O. & Wirth, V. From atmospheric waves to heatwaves: a waveguide perspective for understanding and predicting concurrent, persistent, and extreme extratropical weather. *Bull. Am. Meteorol. Soc.* **103**, E923–E935 (2022).
6. Thompson, V. et al. The 2021 western North America heat wave among the most extreme events ever recorded globally. *Sci. Adv.* **8**, 1–11 (2022).
7. Lin, H., Mo, R. & Vitart, F. The 2021 Western North American heatwave and its subseasonal predictions. *Geophys. Res. Lett.* **49**, 1–10 (2022).
8. White, R. H. et al. The unprecedented Pacific Northwest heatwave of June 2021. *Nat. Commun.* **14**, 727 (2023).
9. Zhang, X. et al. Increased impact of heat domes on 2021-like heat extremes in North America under global warming. *Nat. Commun.* **14**, 1690 (2023).
10. Bartusek, S., Kornhuber, K. & Ting, M. 2021 North American heatwave amplified by climate change-driven nonlinear interactions. *Nat. Clim. Chang.* **12**, 1143–1150 (2022).
11. Benfield, A. *Global Catastrophe Recap September 2021*. http://thoughtleadership.aonbenfield.com/Documents/20190508-analytics-if-april-global-recap.pdf (2021).
12. World Meteorological Organization. *State of the Global Climate WMO Provisional Report*. https://public.wmo.int/en/our-mandate/climate/wmo-statement-state-of-global-climate (2022).
13. Trenberth, K. E. & Branstator, G. Issues in establishing causes of the 1988 drought over North America. *J. Clim.* **5**, 159–172 (1992).
14. Robine, J. et al. Death toll exceeded 70,000 in Europe during the summer of 2003. *C. R. Biol.* **331**, 171–178 (2008).
15. Petoukhov, V., Rahmstorf, S., Petri, S. & Schellnhuber, H. J. Quasiresonant amplification of planetary waves and recent Northern Hemisphere weather extremes. *Proc. Natl Acad. Sci. USA* **110**, 5336–5341 (2013).
16. Trenberth, K. E. & Guillemot, C. J. Physical processes involved in the 1988 drought and 1993 floods in North America. *J. Clim.* **9**, 1288–1298 (1996).
17. Brandefelt, J. & Körnich, H. Northern Hemisphere stationary waves in future climate projections. *J. Clim.* **21**, 6341–6353 (2008).
18. Inatsu, M., Mukougawa, H. & Xie, S. P. Stationary eddy response to surface boundary forcing: Idealized GCM experiments. *J. Atmos. Sci.* **59**, 1898–1915 (2002).

19. Stephenson, D. B. & Held, I. M. GCM response of northern winter stationary waves and storm tracks to increasing amounts of carbon dioxide. *J. Clim.* **6**, 1859–1870 (1993).
20. Ting, M. & Yu, L. Steady response to tropical heating in wavy linear and nonlinear baroclinic models. *J. Atmos. Sci.* **55**, 3565–3582 (1998).
21. Wang, L. & Kushner, P. J. Diagnosing the stratosphere-troposphere stationary wave response to climate change in a general circulation model. *J. Geophys. Res. Atmos.* **116**, 1–16 (2011).
22. Joseph, R., Ting, M. & Kushner, P. J. The global stationary wave response to climate change in a coupled GCM. *J. Clim.* **17**, 540–556 (2004).
23. Ting, M. Maintenance of northern summer stationary waves in a GCM. *J. Atmos. Sci.* **51**, 3286–3308 (1994).
24. Levine, X. J. & Boos, W. R. Sensitivity of subtropical stationary circulations to global warming in climate models: a baroclinic Rossby gyre theory. *Clim. Dyn.* **52**, 4873–4890 (2019).
25. Seager, R., Naik, N. & Vecchi, G. A. Thermodynamic and dynamic mechanisms for large-scale changes in the hydrological cycle in response to global warming. *J. Clim.* **23**, 4651–4668 (2010).
26. Wills, R. C. & Schneider, T. Full access how stationary eddies shape changes in the hydrological cycle: Zonally asymmetric experiments in an idealized GCM. *J. Clim.* **29**, 3161–3179 (2016).
27. Wills, R. C., Byrne, M. P. & Schneider, T. Thermodynamic and dynamic controls on changes in the zonally anomalous hydrological cycle. *Geophys. Res. Lett.* **43**, 4640–4649 (2016).
28. Pascale, S. et al. Weakening of the North American monsoon with global warming. *Nat. Clim. Chang.* **7**, 806–812 (2017).
29. Baker, H. S. et al. Forced summer stationary waves: the opposing effects of direct radiative forcing and sea surface warming. *Clim. Dyn.* **53**, 4291–4309 (2019).
30. Shaw, T. A. & Voigt, A. Tug of war on summertime circulation between radiative forcing and sea surface warming. *Nat. Geosci.* **8**, 560–566 (2015).
31. Teng, H., Branstator, G., Tawfik, A. B. & Callaghan, P. Circumglobal response to prescribed soil moisture over North America. *J. Clim.* **32**, 4525–4545 (2019).
32. Kautz, L. A. et al. Atmospheric blocking and weather extremes over the Euro-Atlantic sector - a review. *Weather Clim. Dyn.* **3**, 305–336 (2022).
33. Balaguru, K. et al. Increased U.S. coastal hurricane risk under climate change. *Sci. Adv.* **9**, eadf0259 (2023).
34. Gill, A. E. Some simple solutions for heat-induced tropical circulation. *Q. J. R. Meteorol. Soc.* **106**, 447–462 (1980).
35. Garfinkel, C. I., White, I. P., Gerber, E. P., Adam, O. & Jucker, M. Nonlinear interaction between the drivers of the monsoon and summertime stationary waves. *Geophys. Res. Lett.* **48**, 1–11 (2021).
36. Henderson, S. A. & Maloney, E. D. The impact of the Madden-Julian oscillation on high-latitude winter blocking during El Niño-Southern Oscillation events. *J. Clim.* **31**, 5293–5318 (2018).
37. Hoskins, B. J. & Ambrizzi, T. Rossby wave propagation on a realistic longitudinally varying flow. *J. Atmos. Sci.* **50**, 1661–1671 (1993).
38. Zhou, W., Leung, L. R. & Lu, J. Seasonally and regionally dependent shifts of the atmospheric westerly jets under global warming. *J. Clim.* **35**, 5433–5447 (2022).
39. Sardeshmukh, P. D. & Hoskins, B. J. The generation of global rotational flow by steady idealized tropical divergence. *J. Atmos. Sci.* **45**, 1228–1251 (1988).
40. Xie, S.-P. et al. Global warming pattern formation: sea surface temperature and rainfall. *J. Clim.* **23**, 966–986 (2010).
41. Zhou, W., Leung, L. R., Lu, J., Yang, D. & Song, F. Contrasting recent and future ITCZ changes from distinct tropical warming patterns. *Geophys. Res. Lett.* **47**, 1–12 (2020).
42. Chen, L., Li, T. & Yu, Y. Causes of strengthening and weakening of ENSO amplitude under global warming in four CMIP5 models*. *J. Clim.* **28**, 3250–3274 (2015).
43. Seager, R. et al. Strengthening tropical Pacific zonal sea surface temperature gradient consistent with rising greenhouse gases. *Nat. Clim. Chang.* **9**, 517–522 (2019).
44. Kohyama, T., Hartmann, D. L. & Battisti, D. S. La Niña-like mean-state response to global warming and potential oceanic roles. *J. Clim.* **30**, 4207–4225 (2017).
45. Hersbach, H. et al. Global reanalysis: goodbye ERA-Interim, hello ERA5. *Meteorology* **159**, 17–24 (2019).
46. Eyring, V. et al. Overview of the coupled model intercomparison project phase 6 (CMIP6) experimental design and organization. *Geosci. Model Dev.* **9**, 1937–1958 (2016).
47. O'Neill, B. C. et al. The Scenario Model Intercomparison Project (ScenarioMIP) for CMIP6. *Geosci. Model Dev.* **9**, 3461–3482 (2016).
48. Held, I. M. & Soden, B. J. Robust response of the hydrological cycle to global warming. *J. Clim.* **19**, 16 (2006).
49. Hoskins, B. J. et al. *Diagnostics of the Global Atmospheric Circulation Based on ECMWF Analyses 1979–1989* (World Meteorological Organization, 1989).
50. Nigam, S. On the dynamical basis for the Asian summer monsoon rainfall-El Niño relationship. *J. Clim.* **7**, 1750–1771 (1994).
51. Chan, S. C. & Nigam, S. Residual diagnosis of diabatic heating from ERA-40 and NCEP reanalyses: Intercomparisons with TRMM. *J. Clim.* **22**, 414–428 (2009).
52. Karoly, D. J. Rossby wave propagation in a barotropic atmosphere. *Dyn. Atmos. Ocean.* **7**, 111–125 (1983).
53. Plumb, R. A. On the three-dimensional propagation of stationary waves. *J. Atmos. Sci.* **42**, 217–229 (1985).
54. Li, Y., Li, J., Jin, F. F. & Zhao, S. Interhemispheric propagation of stationary Rossby waves in a horizontally nonuniform background flow. *J. Atmos. Sci.* **72**, 3233–3256 (2015).
55. Zhao, S., Li, J. & Li, Y. Dynamics of an interhemispheric teleconnection across the critical latitude through a southerly duct during boreal winter. *J. Clim.* **28**, 7437–7456 (2015).
56. Press, W. H., Teukolsky, S. A., Vetterling, W. T. & Flannery, B. P. In *Numerical Recipes in Fortran 77: The Art of Scientific Computing* 704–708 (Cambridge University Press, 1992).

ACKNOWLEDGEMENTS

This study is supported by Office of Science, U.S. Department of Energy (DOE) Biological and Environmental Research as part of the Regional and Global Model Analysis program area. The Pacific Northwest National Laboratory (PNNL) is operated for DOE by Battelle Memorial Institute under contract DE-AC05-76RLO1830. We are grateful to Dr. Mingfang Ting for developing and providing the code of the Stationary Wave Model. We acknowledge Dr. Yanjie Li and Dr. Sen Zhao for developing the ray tracing technique and thank Dr. Koichi Sakaguchi for improving and sharing the tracing code. We also thank the World Climate Research Programme's Working Group on Coupled Modeling, which is responsible for CMIP6, and the climate modeling groups (listed in Supplementary Tables 1 and 2).

AUTHOR CONTRIBUTIONS

J.L. and Z.C. designed the research. Z.C. performed the analysis and drafted the manuscript. Z.C. and C.-C.C. conducted the simulations of Stationary Wave Model. J.L., C.-C.C., S.L. and L.R.L. provided comments and revised the manuscript. All the co-authors contributed to scientific interpretations and helped to improve the manuscript.

COMPETING INTERESTS

The authors declare no competing interests.

ADDITIONAL INFORMATION

Supplementary information The online version contains supplementary material available at https://doi.org/10.1038/s41612-023-00511-2.

Correspondence and requests for materials should be addressed to Ziming Chen or Jian Lu.

Reprints and permission information is available at http://www.nature.com/reprints

Publisher's note Springer Nature remains neutral with regard to jurisdictional claims in published maps and institutional affiliations.